光学学报

界面种子层修饰策略制备高性能 $CsPbIBr_2$ 光电探测器

舒鑫[1]，鹿颖申[1]，张子发[1]，康家兴[1]，袁翔[1]，洪峰[1,2]，徐闰[2,3]，马忠权[1]，徐飞[1,2*]

[1]上海大学物理系，上海市高温超导重点实验室，上海 200444；

[2]上海大学（浙江）高端装备基础件材料研究院，浙江 嘉善 314113；

[3]上海大学电子信息材料系，上海 200444

摘要 在相对湿度低于90%(<90% RH)的大气环境下，通过界面种子层修饰策略，利用气动喷涂法制备出高结晶度、界面接触良好、结构稳定的 $CsPbIBr_2$ 厚膜。界面种子层的引入对 $CsPbIBr_2$ 厚膜的光学带隙(2.10～2.12 eV)没有太大的影响，但明显增强了其对光的吸收和发射，并且荧光寿命也明显延长(从0.95 ns到4.49 ns)。由此厚膜制备的二极管型光电探测器(p-n $CsPbIBr_2$-ITO)具有非常低的暗电流(5.70×10^{-10} A)，并且展示出高效的光电探测性能：高开关比(1.8×10^4)以及微秒级别的响应时间(上升时间和下降时间分别为9 μs、13 μs)。当未封装的 $CsPbIBr_2$ 光电探测器处在<90% RH的大气环境下，其表现出强的抗水抗氧能力：储存60 d后，其仍能保持初始开关比的83%。所提方法为在大气环境下制备低成本、高性能、长效稳定的二极管型 $CsPbIBr_2$ 光电探测器提供了一种有效的途径。

关键词 探测器；二极管型光电探测器；界面种子层；大气环境；气动喷涂

中图分类号 TN364 **文献标志码** A **DOI**：10.3788/AOS230496

1 引 言

光电探测器可以将光信号转换成电信号，在图像传感、光通信、环境监测、生物检测等领域得到广泛应用[1-8]。近年来，全无机金属卤化物钙钛矿 $CsPbIBr_2$ 由于具有良好的光电探测性能，在光电探测领域受到了广泛关注[9-11]。

$CsPbIBr_2$ 材料易受环境湿度影响，一般是在手套箱中制备[12-16]。通常使用添加剂、界面层等手段，改善 $CsPbIBr_2$ 光电探测器的性能和稳定性：在手套箱中将碘化银(AgI)引入前驱液后，制备得到的 $CsPbIBr_2$ 薄膜表面形貌平整、结晶度高，其光电探测器暗电流密度明显降低(从 4.44×10^{-5} A/cm^2 降到 9.71×10^{-6} A/cm^2)、开关比提高(1×10^1)、响应时间(即探测器分别达到稳态值的90% 和下降到10% 所需的时间)下降(从43.7、47.2 μs分别降到22.4、25.7 μs)[13]；或者通过溶液调控可以实现在低湿度环境(相对湿度为30%，即30% RH)中制备，如Du等[10]将硫脲添加到前驱液，促进了 $CsPbIBr_2/TiO_2$ 界面上氢键的形成，加强了界面间的电荷提取，实验结果表明，未封装的器件在10% RH的环境中储存56 d后，仍能保持82.8%的初始性能。利用界面层也可以实现 $CsPbIBr_2$ 光电探测器性能的提升。例如，在手套箱中利用聚乙烯亚胺(PEI)在FTO/$CsPbIBr_2$/C光电探测器中进行界面修饰，优化后的暗电流降低了两个数量级(从 2.20×10^{-7} A到 2.03×10^{-9} A)，响应时间从1.70 μs降为1.21 μs[16]。相似地，将 Ga_2O_3 作为界面层，优化后的 $CsPbIBr_2$ 光电探测器暗电流也降低了约两个数量级(从 1.15×10^{-7} A到 4.19×10^{-9} A)[14]。上述研究说明了界面层具有促进钙钛矿吸收层晶体生长、提高结晶度以及抑制载流子复合的作用。然而，在大气环境中通过修饰界面种子层制备钙钛矿光电探测器的相关研究成果仍鲜有报道。

本实验在<90% RH的大气环境下，通过引入界面种子层，结合气动喷涂法，制备出高结晶质量的 $CsPbIBr_2$ 厚膜。界面种子层修饰策略对 $CsPbIBr_2$ 厚膜的光学带隙(2.10～2.12 eV)没有太大的影响，但明显增强了厚膜对光的吸收和发射，荧光寿命也明显增加(0.95～4.49 ns)。在此基础上，制备出未封装的 $CsPbIBr_2$ 光电探测器，其展示出低暗电流(5.70×10^{-10} A)、高开关比(1.8×10^4)、微秒级别的响应时间(9、13 μs)以及长效的稳定性(即在<90% RH的大气环境下，储存60 d后仍能保持初始开关比的83%)。本实验方法为在大气环境下制备高性能、长效稳定的

收稿日期：2023-02-03；**修回日期**：2023-02-27；**录用日期**：2023-03-20；**网络首发日期**：2023-04-01

基金项目：国家自然科学基金(12175131，61874070，61874027，11527805，11905133)

通信作者：*feixu@shu.edu.cn

$CsPbIBr_2$光电探测器提供了一种有效的途径。

2 实验部分

2.1 材料与前驱液配制

本实验使用的材料包括溴化铯(CsI,纯度为99.9%)、溴化铅($PbBr_2$,纯度为99.9%)、二甲基亚砜(DMSO,纯度为99.9%)、N,N-二甲基甲酰胺(DMF,纯度为99.9%)和金丝(Au,纯度为99.999%)。所有化学品均按原规格使用,无需进一步纯化。$CsPbIBr_2$前驱液配制如下:将不同物质的量(0.1、0.2、0.3、0.4 mmol)的CsI和$PbBr_2$粉末按1∶1的比例加入DMSO(0.5 mL)和DMF(0.5 mL)溶剂中进行搅拌,直至完全溶解。用于气动喷涂法制备$CsPbIBr_2$厚膜的前驱液浓度为0.4 mol/L,用于旋涂法制备界面种子层的前驱液浓度分别为0.1、0.2、0.3、0.4 mol/L。

2.2 光电探测器制备

$CsPbIBr_2$光电探测器采用二极管型p-n $CsPbIBr_2$-ITO结构,即Au/ITO/$CsPbIBr_2$/Au。首先,将ITO衬底依次在丙酮溶液、无水乙醇溶液和去离子水中超声清洗,并将清洗后的衬底使用氮气吹干,再进行15 min的紫外臭氧处理。然后,将不同浓度的$CsPbIBr_2$前驱液滴在预处理后的衬底上,先以500 r/min的转速旋转10 s,再以3000 r/min的转速旋转25 s,之后将其放在150 ℃加热台上30 s得到$CsPbIBr_2$界面种子层。$CsPbIBr_2$厚膜是利用气动喷涂法制备的。制备过程中,厚膜始终处于150 ℃的加热台上。喷涂结束后,退火过程设定为梯度退火,降温梯度为−2 ℃/min。最后,在1×10^{-3} Pa的高真空条件下,在$CsPbIBr_2$厚膜上蒸镀100 nm厚的金电极,电极图案为点电极,有效面积为0.785 mm^2。为了描述简化,将未进行界面种子层修饰的$CsPbIBr_2$厚膜(器件)命名为对照组厚膜(器件),将进行修饰的$CsPbIBr_2$厚膜(器件)命名为修饰组厚膜(器件),并按前驱液浓度分别命名为0.1、0.2、0.3、0.4 mol/L修饰厚膜(器件)。

2.3 测试和表征

使用第一性原理软件包VASP的HSE06杂化泛函计算能带结构[17]。采用型号为Hitachi SU8020的扫描电子显微镜(SEM)观测厚膜表面和截面形貌。采用帕纳科公司的X'Pert Pro型X射线衍射仪(XRD)测量厚膜晶体结构,X射线源是Cu的Kα线($\lambda_{K\alpha}$=1.54056 Å)。采用TU-1901型双光束紫外-可见分光光度计测量厚膜吸收光谱。采用自行搭建的光电集成测量系统(激光的激发波长为405 nm)测量厚膜光致发光光谱(PL)。对于时间分辨PL谱(TRPL),采用405 nm激光作为激发源,通过相关光子计数法采集数据。在暗光和光照下测量器件的电流-电压(I-V)曲线和响应时间曲线,光源为405 nm激光器,光功率在10 μW~100 mW范围可调,光斑面积约为0.2 cm^2。通过固定频率的脉冲激光测试光电流的上升沿和下降沿,从而得到响应时间曲线,其中激光波长为405 nm,强度为30 μW,脉冲频率为50 Hz。

3 分析与讨论

为了从形貌和相结构上了解界面种子层对$CsPbIBr_2$厚膜的影响,进行了SEM和XRD测试。由于界面种子层的引入,与表面晶粒尺寸小且存在大量孔洞的对照组厚膜相比,修饰组厚膜的致密性明显增强,尤其是0.3 mol/L修饰厚膜表面形成均匀致密的大尺寸晶粒[图1(a)],这将降低由孔洞引起的漏电流,改善界面复合效果,从而提高器件性能。进一步的截面观察发现,对照组厚膜在竖直方向上晶粒杂乱、界面接触差,而修饰组厚膜界面接触明显改善,尤其是0.3 mol/L修饰厚膜呈明显的柱状生长[图1(b)],这意味着在电子-空穴对收集方向上几乎没有晶界,有利于载流子的收集[18]。对照组厚膜的XRD谱线出现3个主要的衍射峰,分别对应于α相的(100)、(110)和(200)衍射面[19];同时也存在一些强度小的衍射峰,对应于(210)、(211)衍射面;引入界面种子层后,修饰组厚膜的(110)衍射面峰强度明显增大,特别是0.3 mol/L修饰厚膜显示出明显的择优生长[图1(c)]。一般地,利用气动喷涂法制备$CsPbIBr_2$厚膜的过程大体可以分为4个阶段。当前驱液喷洒到衬底时,最初保持在溶液状态(阶段1)。由于衬底处于加热台上,溶液中的有机溶剂DMF、DMSO逐渐挥发。根据成核动力学,晶胚达到临界成核半径后,克服了对应的吉布斯自由能(原子核能保持稳定存在而不溶解在溶液中时所需的自由能),于是开始成核与生长(阶段2)。当薄膜中的配位溶剂开始蒸发,晶体随之快速生长(阶段3)。在连续喷涂下,晶粒由于具有较高的表面能,会发生溶解再结晶,最终制备得到平整的厚膜(阶段4)。其中,成核行为一旦开始将十分迅速并且难以控制。而界面种子层的主要作用是在成核阶段充当成核点,促进液相和固相之间的动态平衡,并降低$CsPbIBr_2$厚膜的形成能,提供有利于$CsPbIBr_2$晶核生长的动力学条件[20],从而改善晶体的生长。从这个意义上说,引入界面种子层后可改善传统喷涂法制备厚膜工作中晶体结晶不受控制的问题,通过界面修饰可制备出表面形貌致密、界面接触良好、结晶度高的$CsPbIBr_2$厚膜。

图2所示为5组$CsPbIBr_2$厚膜的光学表征。从图2(a)所示的能带图可以看出,价带顶和导带底都位于倒空间的A点(0.5,0.5,0.5),表明$CsPbIBr_2$是直接带隙半导体材料,计算得到其带隙值为2.10 eV,接近实验测试得到的光学带隙。对于直接带隙半导体,可以通过Tauc方程拟合吸收系数得到材料的光学带隙[21],公式为

$$(\alpha h\nu)^2 \propto (h\nu - E_g), \tag{1}$$

式中:h为普朗克常数;ν为光频率。进行线性拟合得

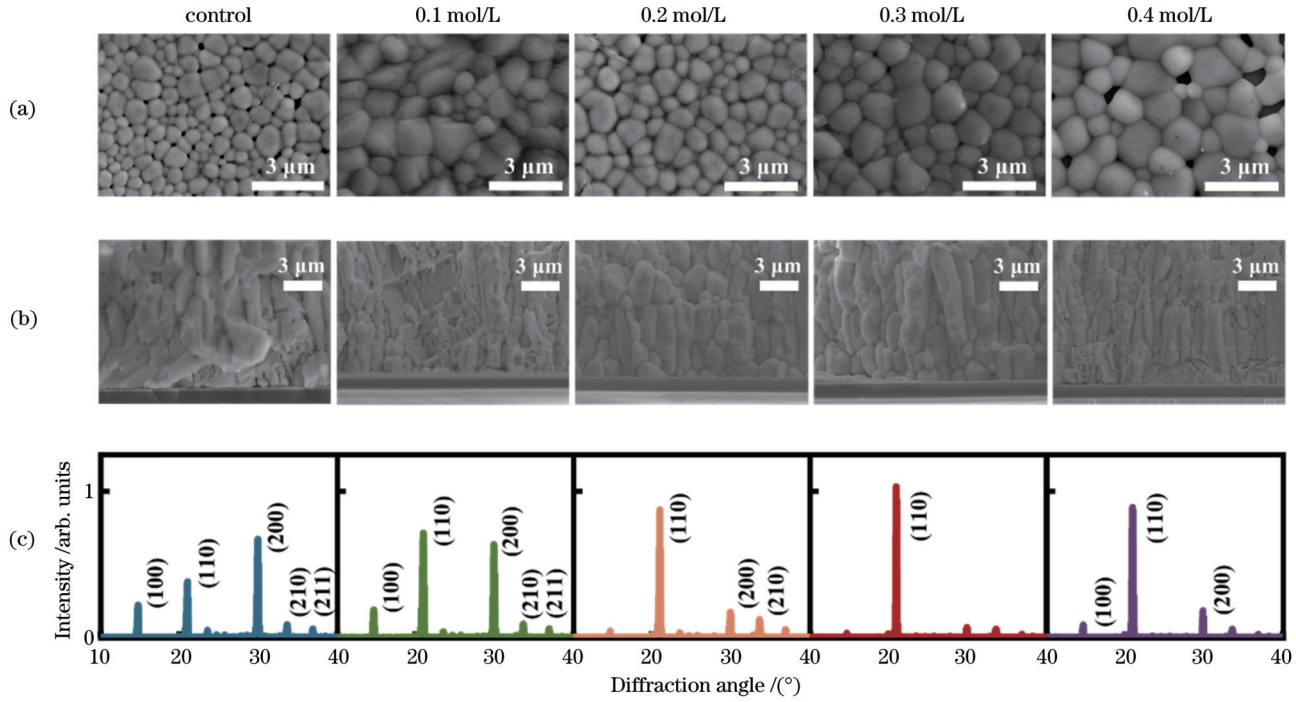

图 1　对照组和修饰组厚膜的微观形貌和物相表征。(a)表面 SEM 图;(b)截面 SEM 图;(c) XRD 图谱

Fig. 1　Morphology and phase characterization of control and modified thick films. (a) Top-view of SEM images; (b) cross-section of SEM images; (c) XRD patterns

到的横坐标截距为样品的 E_g,由此得出 5 组厚膜的 E_g 分别为 2.10、2.10、2.12、2.12、2.11 eV[图 2(b)]。此外,修饰组厚膜在整个可见光范围内的对光吸收效果都明显优于对照组厚膜,其中 0.3 mol/L 修饰厚膜对可见光的吸收最强,可能与其形貌改善和结晶度提高有关。在不同浓度的界面种子层中,0.3 mol/L 修饰厚膜 PL 发光峰强度最大[图 2(c)],表明 0.3 mol/L 修饰厚膜中存在更少的缺陷态[22]。$CsPbIBr_2$ 厚膜的 TRPL 光谱可以通过双指数函数进行拟合[23],公式为

$$f(t)=A_1\exp\left(-\frac{t}{\tau_1}\right)+A_2\exp\left(-\frac{t}{\tau_2}\right)+B, \quad (2)$$

式中:τ_1、τ_2 分别为快、慢衰减时间常数;A_1、A_2 分别为 τ_1、τ_2 对应的衰减振幅。TRPL 光谱的拟合结果见表 1,发现荧光寿命从 0.95 ns 增加到 4.49 ns,这有利于 $CsPbIBr_2$ 厚膜的载流子提取与电荷收集[图 2(d)]。

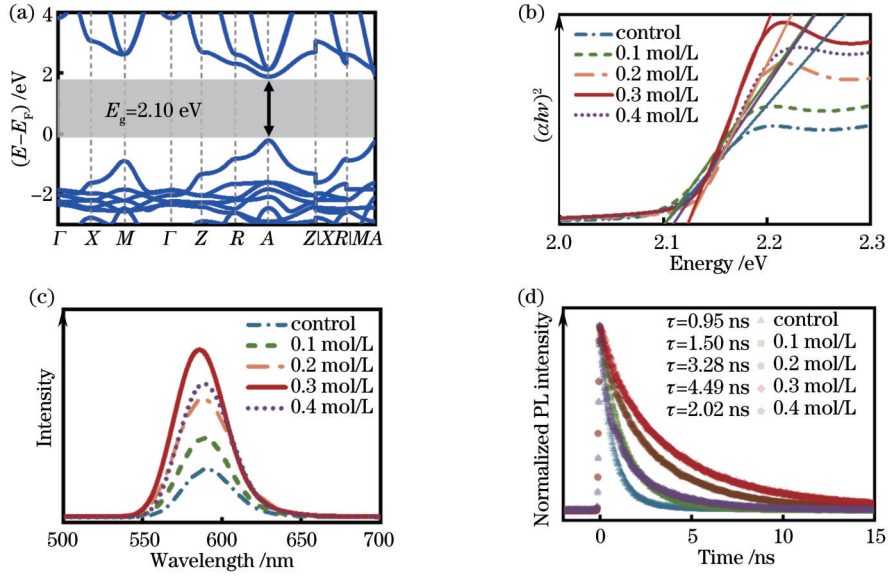

图 2　对照组与修饰组厚膜的光学表征。(a) $CsPbIBr_2$ 能带结构;(b)紫外-可见吸收光谱;(c) PL 光谱;(d) TRPL 光谱

Fig. 2　Optical characterization of control and modified thick films. (a) $CsPbIBr_2$ band structure; (b) UV-Vis absorption spectra; (c) PL spectra; (d) TRPL spectra

表 1　对照组与修饰组厚膜 TRPL 光谱的拟合参数

Table 1　Fitting parameters of TRPL spectra in the control and modified thick films

Sample	A_1	τ_1 /ns	A_2	τ_2 /ns	τ_{ave} /ns
Control	0.66	0.53	0.34	1.29	0.95
0.1 mol/L	0.36	0.76	0.64	1.69	1.50
0.2 mol/L	0.32	0.92	0.68	3.57	3.28
0.3 mol/L	0.33	1.38	0.67	4.92	4.49
0.4 mol/L	0.48	0.40	0.52	2.28	2.02

为了探究界面种子层对光电性能的影响，研究了二极管型(p-n $CsPbIBr_2$-ITO)器件在暗光和光照下的 *I-V* 曲线以及时间响应曲线，结果见图 3。其中，$CsPbIBr_2$是弱 p 型半导体，ITO 是 n 型半导体。当二者接触时，由于功函数不同，载流子会发生热运动，产生内建电场，并且电场主要分布在 $CsPbIBr_2$区。从暗光的 *I-V* 曲线来看，与对照组器件的暗电流(2.05×10^{-7} A)相比，修饰组器件的暗电流降低了 1～3 个数量级[图 3(a)]。值得注意的是，0.3 mol/L 修饰器件的暗电流值下降最为明显，降为 5.70×10^{-10} A，低于大部分的 $CsPbIBr_2$钙钛矿光电探测器的暗电流值(2.66×10^{-6}～3.12×10^{-10} A)[9-16]。这可能是因为种子层减少了 ITO/$CsPbIBr_2$界面的复合中心数量，同时也改善了体内的结晶质量，从而降低了器件的漏电流[24-26]。从 *I-V* 曲线所得的结果与 SEM 和 XRD 的结果一致。在光照条件下：对照组器件的光响应较差，开关比为 490；修饰组的开关比明显增大，尤其是 0.3 mol/L 修饰器件的开关比高达 1.8×10^4。为了分析线性动态范围(R_{LD})和功率指数 n 的变化，测量了不同光照强度下的对照组器件和 0.3 mol/L 修饰器件的 *I-V* 曲线和光响应曲线[图 3(b)～(e)]。对照组器件在光功率密度增加到 5×10^{-3} W/cm^{2}时光电流趋于饱和，而 0.3 mol/L 修饰器件则在光功率密度增加到 5×10^{-1} W/cm^{2}后光电流依然有线性响应。由此拟合幂律曲线，发现两组器件的 n 从 0.60 增长到 0.87，可见修饰组的 n 值更接近理想值 1。这说明 0.3 mol/L 修饰器件对光强有更好的响应，再次证明了该厚膜中陷阱态较少[27]。进一步计算了器件的 R_{LD}，它的定义为光电流与入射光功率呈线性变化的范围，计算公式为

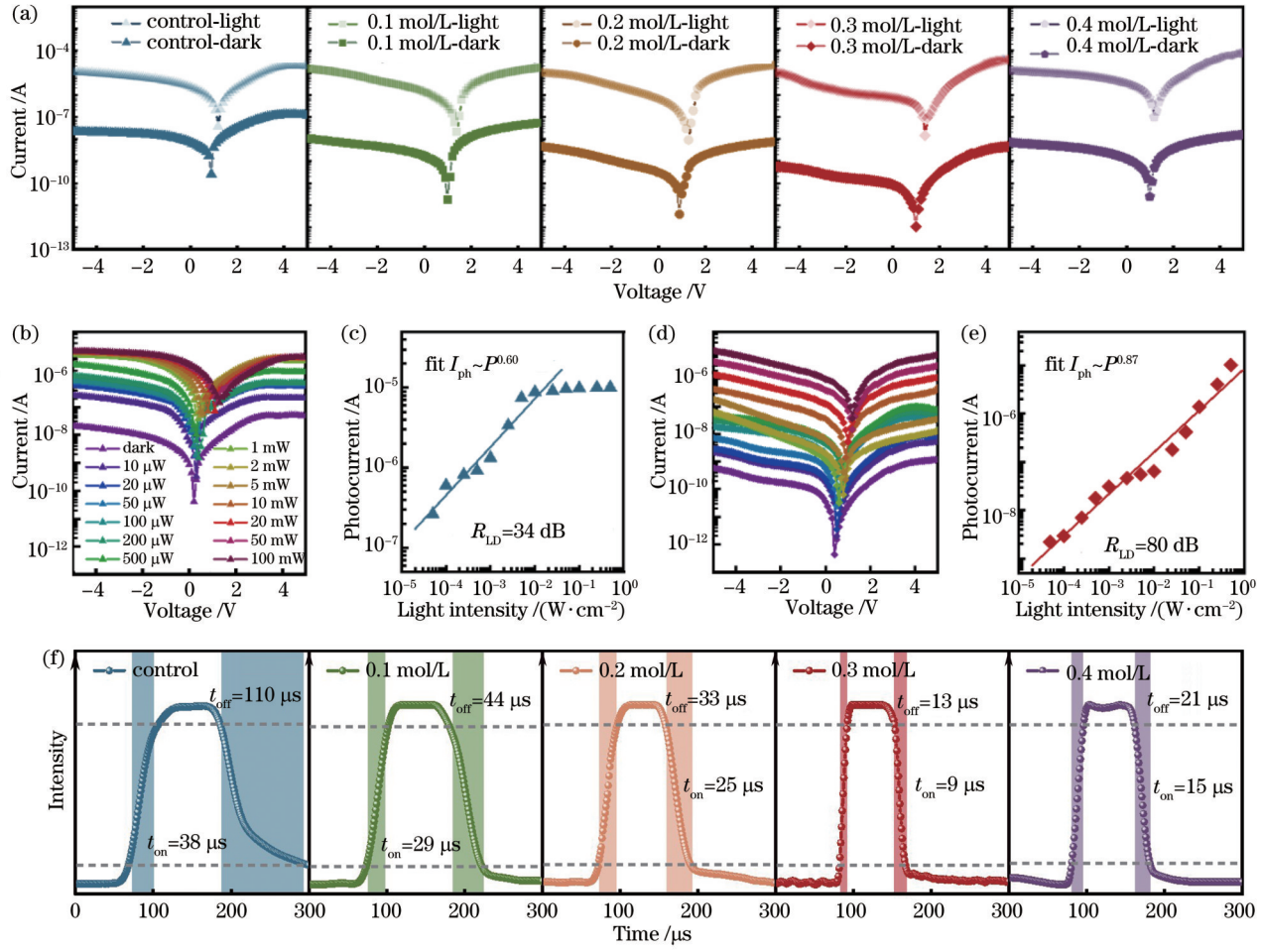

图 3　对照组和修饰组器件的光电表征。(a) *I-V* 曲线；(b)(c)对照组器件光电流随入射光功率的变化关系；(d)(e) 0.3 mol/L 修饰器件光电流随入射光功率的变化关系；(f)时间响应

Fig. 3　Photoelectric characterization of control and modified thick films. (a) *I-V* characteristics; (b)(c) current of control thick film changed with input optical power; (d)(e) current of 0.3 mol/L modified thick film changed with input optical power; (d) time response

$$R_{LD}=20\times\log\frac{P_{max}}{P_{min}},\tag{3}$$

式中：P_{max}为入射光功率的最大值；P_{min}为入射光功率的最小值。对照组器件的R_{LD}仅为34 dB，0.3 mol/L修饰器件的R_{LD}则展宽至80 dB，并且此时器件光电流依然没有饱和，表明0.3 mol/L修饰器件存在更大的光响应范围。响应时间也是评估光电探测器灵敏度的关键参数。与对照组器件的上升时间t_{on}(35 μs)和下降时间t_{off}(113 μs)相比，修饰组器件的响应时间明显缩短[图3(f)]，这是因为修饰组器件的电荷分离和收集能力提升。0.3 mol/L修饰器件的上升时间和下降时间更是缩短为9 μs和13 μs，优于很多硅基和钙钛矿光电探测器的结果(毫秒、亚毫秒级别)[28-31]。

为了确定对照组和0.3 mol/L修饰厚膜及其器件的稳定性，对两组厚膜进行了长达60 d的拍照跟踪，并对器件的开关比进行了连续测量(图4)。在<90% RH的大气环境中，对照组厚膜的稳定性明显较差：第30天时样品的颜色已变成黄棕色，推测已变为δ相。相比之下，0.3 mol/L修饰厚膜在60 d内颜色未发生明显变化。这可能是因为对照组厚膜存在孔洞，增加了样品与空气中水分子和氧分子的接触，从而导致其颜色急速变化。与此相应，对照组器件的开关比出现显著衰减。在60 d后，0.3 mol/L修饰器件仍具有

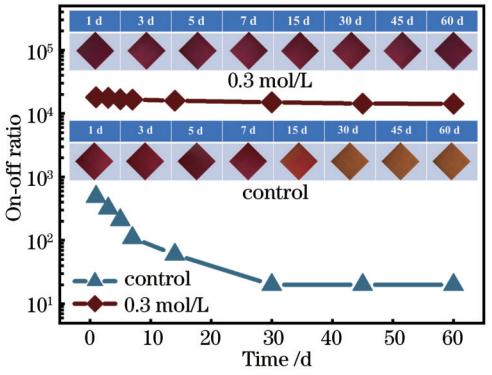

图4　对照组和0.3 mol/L修饰厚膜形貌以及器件的开关比随时间的变化

Fig. 4　Morphologies of control and 0.3 mol/L modified thick film and the on-off ratio of the devices changed with time

1.5×10⁴的高开关比，保留了初始开关比的83%，这证实了0.3 mol/L修饰器件在大气环境下具有长效稳定性。表2所示为采用界面种子层策略的$CsPbIBr_2$光电探测器与其他$CsPbIBr_2$探测器的性能比较，其中一个响应时间是通过拟合单指数衰减的瞬态光电流曲线得到的，两个响应时间是通过固定频率的脉冲激光测试上升沿和下降沿的光电流得到的。表2的数据说明了所制备的0.3 mol/L修饰器件在$CsPbIBr_2$光电探测器中综合性能表现较好，具有巨大的应用潜力。

表2　采用界面种子层策略的$CsPbIBr_2$光电探测器与其他$CsPbIBr_2$探测器的性能比较

Table 2　Performance comparison of inorganic $CsPbIBr_2$ photodetector using interfacial seed layer with other reports

Device structure	Preparation environment	Response time /μs	Dark current /(10^{-10} A)	On-off ratio	Stability	Ref.
FTO/TiO_2/$CsPbIBr_2$/carbon	Glovebox	2.07	3.12	—	—	[12]
FTO/TiO_2/Ga_2O_3/$CsPbIBr_2$/carbon	Glovebox	1.83	41.50	—	—	[14]
ITO/TiO_2/$CsPbIBr_2$/Spiro/Au	Glovebox	22.4, 25.7	5826.00	—	—	[13]
FTO/$CsPbIBr_2$/carbon	Glovebox	1.21	20.30	—	—	[16]
ITO/$CsPbIBr_2$/Au	Glovebox	320, 230	24.50	10^3	—	[15]
Au/$CsPbIBr_2$/Au	Air, 35%-45%RH	100, 140	—	10^4	97%, 30 d	[11]
FTO/$CsPbIBr_2$/Au	Air, 30%RH	2900, 6500	—	10^5	82%, 56 d	[10]
ITO/$CsPbIBr_2$/Au	Air, 40%-60%RH	20, 21	16.00	10^2	81%, 70 d	[9]
Au/ITO/$CsPbIBr_2$/Au	Air, <90% RH	9, 13	5.70	10^4	83%, 60 d	This work

4　结　　论

在<90% RH的大气环境下，通过引入$CsPbIBr_2$界面种子层，结合气动喷涂法，制备出高质量的$CsPbIBr_2$厚膜。其中界面种子层提高了厚膜的结晶质量，促使$CsPbIBr_2$厚膜的结晶度、界面接触以及结构稳定性得到提升。界面种子层对$CsPbIBr_2$厚膜的光学带隙没有太大的影响，但明显增强了其对光的吸收和发射效应，荧光寿命明显延长。由此制备的未封装光电二极管型$CsPbIBr_2$光电探测器(p-n $CsPbIBr_2$-ITO)展示出较低的暗电流(5.70×10^{-10} A)，并具有高效的光电探测性能(开关比为1.8×10⁴)、微秒级别的响应时间(t_{on}、t_{off}分别为9 μs和13 μs)以及优异的电学稳定性(在<90% RH的大气环境下，储存60 d后，仍能保持初始开关比的83%)。本研究为在大气环境中制备高性能和长效稳定的$CsPbIBr_2$钙钛矿光电探测器提供了简单而有效的方法。

参　考　文　献

[1] 陈红云，鲁玉，李辰，等. 多层$PtSe_2$/TiO_2纳米棒肖特基结紫外光电探测器[J]. 光学学报，2020，40(20)：2025001.
Chen H Y，Lu Y，Li C，et al. Multilayer $PtSe_2$/TiO_2 NRs Schottky junction for UV photodetector[J]. Acta Optica Sinica，

2020, 40(20): 2025001.

[2] 胡韩飞, 徐英添, 李莉, 等. 基于溶胶凝胶法制备的 $CuCr_{1-x}Mg_xO_2$/ZnO 纳米棒紫外光电探测器[J]. 光学学报, 2022, 42(14): 1423001.
Hu H F, Xu Y T, Li L, et al. $CuCr_{1-x}Mg_xO_2$/ZnO nanorods UV photodetector prepared by Sol-gel method[J]. Acta Optica Sinica, 2022, 42(14): 1423001.

[3] 杨乐臣, 付凯, 史学舜, 等. 金属-半导体-金属结构 A1GaN/GaN 异质结紫外探测器技术及特性[J]. 光学学报, 2014, 34(s1): s104001.
Yang L C, Fu K, Shi X X, et al. Technology and performance of metal-semiconductor-metal AlGaN/GaN heterostructure ultraviolet photodetector[J]. Acta Optica Sinica, 2014, 34(s1): s104001.

[4] 马文博, 匡翠方, 刘旭, 等. 基于新型金属卤化物半导体和闪烁体的X射线探测与成像研究进展[J]. 光学学报, 2022, 42(17): 1704002.
Ma W B, Kuang C F, Liu X, et al. Research progress of X-ray detection and imaging based on emerging metal halide semiconductors and scintillators[J]. Acta Optica Sinica, 2022, 42(17): 1704002.

[5] 吴刚, 唐利斌, 郝群, 等. 基于Pt/GaN/AlGaN异质结高响应度双波段紫外探测器[J]. 光学学报, 2023, 43(3): 0304002.
Wu G, Tang L B, Hao Q, et al. Dual-band and high-responsivity ultraviolet detector based on Pt/GaN/AlGaN heterojunction [J]. Acta Optica Sinica, 2023, 43(3): 0304002.

[6] 叶志镇, 王凤志, 陈芳, 等. 宽禁带半导体光电材料及其应用研究[J]. 光学学报, 2022, 42(17): 1716001.
Ye Z Z, Wang F Z, Chen F, et al. Wide band gap semiconductor optoelectronic materials and their applications[J]. Acta Optica Sinica, 2022, 42(17): 1716001.

[7] 林亚楠, 吴亚东, 程海洋, 等. $PdSe_2$纳米线薄膜/Si异质结近红外集成光电探测器[J]. 光学学报, 2021, 41(21): 2125001.
Lin Y N, Wu Y D, Cheng H Y, et al. Near-infrared integrated photodetector based on $PdSe_2$ nanowires film/Si heterojunction [J]. Acta Optica Sinica, 2021, 41(21): 2125001.

[8] 翁思远, 蒋大勇, 赵曼. P3HT∶PC61BM作为活性层制备无机/有机异质结光电探测器的研究[J]. 光学学报, 2022, 42(13): 1304001.
Weng S Y, Jiang D Y, Zhao M. P3HT∶PC61BM as active layer for preparation of inorganic/organic heterojunction photodetector[J]. Acta Optica Sinica, 2022, 42(13): 1304001.

[9] 胡紫婷, 舒鑫, 王香, 等. 双配体策略制备大气环境下性能稳定的$CsPbIBr_2$光电探测器[J]. 物理学报, 2022, 71(11): 116801.
Hu Z T, Shu X, Wang X, et al. Air-stable $CsPbIBr_2$ photodetector via dual-ligand-assisted solution strategy[J]. Acta Physica Sinica, 2022, 71(11): 116801.

[10] Du J, Duan J L, Yang X Y, et al. Reducing defect of inorganic perovskite film by sulphur-containing Lewis base for robust photodetectors[J]. Journal of Energy Chemistry, 2021, 61: 163-169.

[11] Liu Z J, Li H, Qin C J, et al. Solution-processed inorganic perovskite flexible photodetectors with high performance[J]. Nanoscale Research Letters, 2019, 14(1): 284-291.

[12] Zhang Z, Zhang W T, Wei Z M, et al. Dipole-templated homogeneous grain growth of $CsPbIBr_2$ films for efficient self-powered, all-inorganic photodetectors[J]. Solar Energy, 2020, 209: 371-378.

[13] Obiozo E V, Ryan A G, Braga C L, et al. Enhanced inorganic $CsPbIBr_2$ perovskite film for a sensitive and rapid response self-powered photodetector[J]. Journal of Physical Chemistry C, 2020, 124(38): 20643-20653.

[14] Zhang Z, Zhang W T, Jiang Q B, et al. High-performance, vacuum-free, and self-powered $CsPbIBr_2$ photodetectors boosted by ultra-wide-bandgap Ga_2O_3 interlayer[J]. IEEE Electron Device Letters, 2020, 41(10): 1532-1535.

[15] Zhang T, Li S B. Self-powered all-inorganic perovskite photodetectors with fast response speed[J]. Nanoscale Research Letters, 2021, 16(1): 6-13.

[16] Zhang Z, Zhang W T, Jiang Q B, et al. Toward high-performance electron/hole-transporting-layer-free, self-powered $CsPbIBr_2$ photodetectors via interfacial engineering[J]. ACS Applied Materials & Interfaces, 2020, 12(5): 6607-6614.

[17] Blochl P E. Projector augmented-wave method[J]. Physical Review B, 1994, 50(24): 17953-17979.

[18] Haruta Y, Wada S, Ikenoue T, et al. Columnar grain growth of lead-free double perovskite using mist deposition method for sensitive X-ray detectors[J]. Crystal Growth & Design, 2021, 21(7): 4030-4037.

[19] Zhu W D, Zhang Z Y, Chai W M, et al. Benign pinholes in $CsPbIBr_2$ absorber film enable efficient carbon-based, all-inorganic perovskite solar cells[J]. ACS Applied Energy Materials, 2019, 2(7): 5254-5262.

[20] Zhao Y C, Tan H R, Yuan H F, et al. Perovskite seeding growth of formamidinium-lead-iodide-based perovskites for efficient and stable solar cells[J]. Nature Communications, 2018, 9(1): 1607-1617.

[21] Birgin E G, Chambouleyron I, Martínez J M. Estimation of the optical constants and the thickness of thin films using unconstrained optimization[J]. Journal of Computational Physics, 1999, 151(2): 862-880.

[22] Xue Q F, Bai Y, Liu M Y, et al. Dual interfacial modifications enable high performance semitransparent perovskite solar cells with large open circuit voltage and fill factor[J]. Advanced Energy Materials, 2017, 7(9): 1602333.

[23] Chen W J, Li D, Chen S S, et al. Spatial distribution recast for organic bulk heterojunctions for high-performance all-inorganic perovskite/organic integrated solar cells[J]. Advanced Energy Materials, 2020, 10(35): 2000851.

[24] Hu W D, Chen X S, Ye Z H, et al. A hybrid surface passivation on HgCdTe long wave infrared detector with *in situ* CdTe deposition and high-density hydrogen plasma modification [J]. Applied Physics Letters, 2011, 99(9): 091101.

[25] Jozwikowska A, Jozwikowski K, Antoszewski J, et al. Generation-recombination effects on dark currents in CdTe-passivated midwave infrared HgCdTe photodiodes[J]. Journal of Applied Physics, 2005, 98(1): 014504.

[26] Yang Z C, Meng W W, Kang J X, et al. Unraveling the defect-dominated broadband emission mechanisms in (001)-preferred two-dimensional layered antimony-halide perovskite film[J]. The Journal of Physical Chemistry Letters, 2022, 13(50): 11736-11744.

[27] Liang Z M, Zeng P Y, Liu P Y, et al. Interface engineering to boost photoresponse performance of self-powered, broad-bandwidth PEDOT: PSS/Si heterojunction photodetector[J]. ACS Applied Materials & Interfaces, 2016, 8(29): 19158-19167.

[28] Chen G S, Feng J G, Gao H F, et al. Stable α-$CsPbI_3$ perovskite nanowire arrays with preferential crystallographic orientation for highly sensitive photodetectors[J]. Advanced Functional Materials, 2019, 29(13): 1808741.

[29] Cui D, Tian C C, Wang Y P, et al. Back-to-back Schottky junction photodetectors based on CVD grown $CsPbBr_3$ microcrystalline striped films[J]. AIP Advances, 2019, 9(12): 125039.

[30] Tsai D S, Lien D H, Tsai M L, et al. Trilayered MoS_2 metal–semiconductor-metal photodetectors: photogain and radiation resistance[J]. IEEE Journal of Selected Topics in Quantum Electronics, 2014, 20(1): 30-35.

[31] Kim H S, Kumar M D, Patel M, et al. High-performing ITO/CuO/n-Si photodetector with ultrafast photoresponse[J]. Sensors and Actuators A, 2016, 252: 35-41.

Preparation of High-Performance $CsPbIBr_2$ Photodetector via Interfacial Seed Layer Modification Strategy

Shu Xin[1], Lu Yingshen[1], Zhang Zifa[1], Kang Jiaxing[1], Yuan Xiang[1], Hong Feng[1,2], Xu Run[2,3], Ma Zhongquan[1], Xu Fei[1,2*]

[1]*Shanghai Key Laboratory of High Temperature Superconductors, Department of Physics, Shanghai University, Shanghai* 200444, *China*;

[2]*Zhejiang Institute of Advanced Materials, Shanghai University, Jiashan* 314113, *Zhejiang, China*;

[3]*Department of Electronic Information Materials, Shanghai University, Shanghai* 200444, *China*

Abstract

Objective Photodetectors can convert incident light into electric signals and are widely used in many fields such as image sensing, optical communication, environmental monitoring, and biological detection. In recent years, all-inorganic metal halide perovskite $CsPbIBr_2$ has been concerned in photoelectric detection due to its high light absorption coefficient, high charge carrier mobility, and low defect density. On the one hand, $CsPbIBr_2$ film is susceptible to ambient humidity, so it is not usually prepared under an atmospheric environment but in glove boxes by methods such as spin coating. On the other hand, on account of uncontrolled nucleation during crystallization, $CsPbIBr_2$ film has poor morphology and crystallinity, which results in weak photoelectric characteristics and instability of its photodetector. In order to overcome these problems, the morphology, crystallinity, and water/oxygen resistance of $CsPbIBr_2$ thick film can be improved by additives and interface layer strategies. In this study, we employ an interfacial seed layer modification strategy under an atmospheric environment with relative humidity (RH) below 90% to prepare one high-quality $CsPbIBr_2$ thick film with high crystallinity, excellent interfacial contact, and stable structure. We hope that our findings can help fabricate low-cost, high-performance, and long-lasting photodiode-type $CsPbIBr_2$ photodetectors under an atmospheric environment.

Methods $CsPbIBr_2$ thick films with controllable thicknesses in the range of 0.5–100 μm are prepared under an atmospheric environment with RH below 90% by pneumatic spraying. Prior to spraying, the interfacial seed layers are formed on the substrates by spin-coating followed by annealing. During spin-coating, the density distribution of the interfacial seed layers is realized by controlling the concentration of precursor solution. In this strategy, the interfacial seed layers act as the nucleating points for crystal growth, which improve the crystallization of the thick films in preparation processing. The morphology and the phase structure of the thick films are analyzed by scanning electron microscopy (SEM) and X-ray diffraction. Compared with the thick film without an interfacial seed layer, these films with interfacial seed layers have high crystallinity, excellent interfacial contact, and stable structure. In order to assess the effect of interfacial seed layers on the optical properties of the thick films, these thick films are investigated by absorption, photoluminescence (PL), and time-resolved PL spectra. In order to verify the feasibility of the thick films for photodetection, their photodiode-type photodetectors of Au/ITO/$CsPbIBr_2$/Au are fabricated and measured. The *I-V* and response time curves of the photodetectors are examined under laser excitation of 405 nm. In order to characterize the long-term stability, tracing measurements on the on-off ratio of the devices are made, and the naked-eye photographs of the corresponding thick films are recorded.

Results and Discussions Compared with the control film with small-size crystal grains and a large number of holes on the surface, the modified films by introducing interfacial seed layers exhibit large-size crystal grains and dense morphology [Fig. 1(a)]. From the cross-sectional SEM images, the improved interfacial contacts between the modified films and the substrates lead to columnar growth features [Fig. 1(b)]. The modified films show a preferred orientation on the (110) diffraction plane, especially for 0.3 mol/L, which is consistent with the SEM results [Fig. 1(c)]. Once seed layers are inserted between the thick films and the substrates, the absorption coefficients and PL peak intensities increase significantly in the whole visible range, and the fluorescence lifetime increases from 0.95 ns to 4.49 ns (Fig. 2). The dark current from the control device to the modified devices decreases from 2.05×10^{-7} to 5.70×10^{-10} A, while the on-off ratio significantly increases from 490 to 1.8×10^4 [Fig. 3(a)]. By fitting the *I-V* curves under light illumination, it is proved that the modified device of 0.3 mol/L has a stronger light response (n=0.87) and larger response range (R_{LD}=80 dB) than the control device (n=0.60 and R_{LD}=34 dB) [Fig. 3(b)-(e)]. The rising and falling time (t_{on} and t_{off}) from the control device to the modified devices decreases from 38 μs to 9 μs and from 110 μs to 13 μs, respectively [Fig. 3(f)]. After lasting 60 days, the modified device of 0.3 mol/L still retains a high on-off ratio of 1.5×10^4, which is 83% of the initial on-off ratio, and the

naked-eye photographs of the thick films do not change significantly (Fig. 4).

Conclusions In this study, under an atmospheric environment with RH below 90%, high-quality $CsPbIBr_2$ thick films are prepared by pneumatic spraying via an interfacial seed layer modification strategy. In this strategy, the interfacial seed layer acts as the nucleating points for crystal growth, which results in the improvement of the crystallinity, interfacial contact, and structural stability of the $CsPbIBr_2$ thick films. Furthermore, the introduction of interfacial seed layers has no significant effect on the optical band gaps of $CsPbIBr_2$ thick films, ranging from 2.10 eV to 2.12 eV. It is worth noting that the absorption coefficient of visible light and the PL intensity are enhanced significantly, and meanwhile the fluorescence lifetime is increased (from 0.95 ns to 4.49 ns). The photodiode-type $CsPbIBr_2$ photodetector (p-n $CsPbIBr_2$-ITO) shows a low dark current (5.70×10^{-10} A) and possesses high-performance photodetection parameters, namely high on-off ratio (1.8×10^4) and microsecond-level response times (9 μs and 13 μs). Moreover, the unpackaged $CsPbIBr_2$ photodetector is strongly resistant to water and oxygen under an atmospheric environment with RH below 90%, which is 83% of the initial on-off ratio after lasting 60 days. These results can provide an effective way to prepare low-cost, high-performance, long-lasting, and stable photodiode-type $CsPbIBr_2$ photodetectors under an atmospheric environment.

Key words detector; photodiode-type photodetector; interfacial seed layer; atmospheric environment; pneumatic spraying